Articles in PresS. J Neurophysiol (December 17, 2008). doi:10.1152/jn.90992.2008

High-Resolution Three-Dimensional Extracellular Recording of Neuronal Activity with Microfabricated Electrode Arrays

Jiangang Du[1], Ingmar H. Riedel-Kruse[1], Janna C. Nawroth[1], Michael L. Roukes[2], Gilles J. Laurent[1], Sotiris C. Masmanidis[1]

1. *Department of Biology, California Institute of Technology, Pasadena, California; and*
2. *Kavli Nanoscience Institute, California Institute of Technology, Pasadena, California*

Running head:

High-resolution 3D extracellular recording

Corresponding author contact information:

Sotiris C. Masmanidis
1200 E. California Blvd.
MC 216-76
Pasadena, CA 91125
USA
E-mail: sotiris@caltech.edu

ABSTRACT

Microelectrode array recordings of neuronal activity present significant opportunities for studying the brain with single cell and spike time precision. However, challenges in device manufacturing constrain dense multisite recordings to two spatial dimensions, whereas access to the three-dimensional (3D) structure of many brain regions appears to remain a challenge. To overcome this limitation, we present two novel recording modalities of silicon-based devices aimed at establishing 3D functionality. First, we fabricated a dual-side electrode array by patterning recording sites on both the front and back of an implantable microstructure. We found that the majority of single-unit spikes could not be simultaneously detected from both sides, suggesting that in addition to providing higher spatial resolution measurements than single-side devices, dual-side arrays also lead to increased recording yield. Second, we obtained recordings along three principal directions with a multilayer array and demonstrated 3D spike source localization within the enclosed measurement space. The large scale integration of such dual-side and multilayer arrays is expected to provide massively parallel recording capabilities in the brain.

INTRODUCTION

Monitoring the interplay of neuronal ensembles in the brain is important for understanding mechanisms underlying learning, memory, and behavior. Using advances in multisite microelectrode fabrication techniques, it is possible to measure the activity of tens to hundreds of neurons in parallel (Buzsáki 2004). Integrated microelectronic circuits are poised to facilitate a transition to even higher recording capacities (Olsson *et al.* 2005). However, significant challenges remain in the development of implantable devices for sampling extracellular neuronal activity with high spatial resolution across a region of interest. Most existing electrode microelectrode arrays are distributed along two spatial dimensions, inherently restricting their ability to capture the dynamics of large neuronal ensembles exhibiting complex connectivity patterns. A method for extending extracellular measurements into the three-dimensional (3D) domain would provide a unique high-resolution functional mapping tool for the brain. Significant effort has thus been made to create implantable microstructures supporting a dense 3D array of recording electrodes (Wise *et al.* 2008).

Microwire arrays (Nicolelis *et al.* 1997), and analogous silicon-based microstructures (Campbell *et al.* 1991), provide limited scope for dense 3D measurements, as their sampling volume is constrained by the availability of only one recording site per wire. An alternative architecture, the planar microelectrode array (Najafi *et al.* 1985), utilizes electrodes arranged on one or more implantable silicon shafts. The principal advantage of this design lies in the ability to simultaneously obtain depth and axial information with a high level of spatial precision. Tests with such devices have demonstrated their effectiveness in densely sampling neuronal activity within a single plane (Csicsvari *et al.* 2003; Blanche *et al.* 2005). Moreover, an extension of the traditional planar architecture has been proposed in the form of double-sided electrodes (Perlin and Wise 2004). These devices contain electrodes on two parallel planes separated by the thickness of the implantable shaft, and manifest a simple, localized 3D recording geometry. The most large scale 3D arrays involve modular assembly of planar arrays using multiple structural layers (Hoogerwerf and Wise 1994; Bai *et al.* 2000; Pang *et al.* 2005; Neves *et al.* 2007; Yao *et al.* 2007). Research on such devices has primarily focused on important aspects of the fabrication process,

insertion into the cortex, and chronic response of tissue to the implant. However, despite achieving impressive levels of device complexity, high spatial resolution extracellular measurements do not appear to have been carried out in 3D with existing neural probe microstructures.

Here, we demonstrate 3D recording in devices created by a silicon fabrication method involving dual-side processing and assembly techniques. The design introduces two new recording functionalities, which were explored *in vivo* with two separate devices. Both device attributes enable 3D extracellular measurements with a high level of spatial and temporal precision. First, we developed a dual-side electrode array by placing separately addressable recording sites on each planar surface of the implant. This allowed us to increase the density of recording sites in the region of interest by twofold. Moreover, our results indicate that conventional single-side arrays may shield spike activity of some neurons facing the other side of the array. Second, we assembled a double-layer probe using a pair of planar microstructures placed 100 μm apart. A unique feature of this device was that the planar recording sites on both layers faced inward, toward the space between the two layers. This enabled us to record, and triangulate the source of, extracellular action potential signals from several sites within the enclosed region.

MATERIALS AND METHODS

Device development

The arrays were built using surface and bulk micromachining techniques. The starting material was a silicon substrate with a thickness of 25±5μm or 50±5 μm, which determined the final device thickness (J. Du *et al.,* in preparation). Gold recording sites (100 μm^2) were patterned on both sides of the substrate, by first defining the features on the front side, then turning the substrate over and repeating the metallization process on the back. The top and bottom insulation layers on each side consisted of 2 μm films of parylene C and thermal oxide, respectively. The silicon device substrate was patterned into its final shape by means of a deep reactive ion etch process. A representative device is shown in Fig. 1A. The shaft dimensions are 4 mm x 70 μm *(l x w),* and its silicon layer thickness is 50 μm, although 25 μm thick

devices were also used in the course of these experiments. The end of each shaft contains eight electrodes on the front as well as the back side (Fig. 1B), and is tapered to facilitate tissue penetration.

Assembly proceeded by flip-chip bonding onto a flexible printed circuit board (PCB) using an anisotropic conductive adhesive film, which permitted current to flow out of plane but remained highly resistive in plane. The flip-chip bonding process entirely eliminated the need for wire bonds in all of our devices. In addition, it resulted in an essentially flat contact profile between the silicon device layer and PCB; this attribute was exploited to connect a PCB to each side of the dual-side array (Fig. 1C), by first flip-chip bonding the contacts on the front side, turning the structure over, and bonding with another PCB to the back side contacts. This novel assembly method raises the prospect for creating modular, three dimensional microstructures. A simple modular device was realized by bonding two carefully aligned silicon layers on each side of a PCB to create a double-layer structure (Figs. 1D, 1E). After assembly, the contact regions were sealed with epoxy. Finally, in order to maintain a high signal-to-noise ratio (SNR) and minimize electrical crosstalk, electrode impedance was reduced from roughly 2.1 MΩ to 0.2-0.25 MΩ with electrodeposited gold. A detailed analysis of crosstalk is presented in the Appendix. The finished devices contained 32 connected recording channels; 16 per side and 16 per layer for the dual-side and double-layer arrays, respectively.

Single-unit and LFP recordings

Acute measurements were carried out in locusts (*Schistocerca americana*), whose antennae and body were fixed, and brain desheathed and perfused with saline (Laurent and Davidowitz 1994). Signals were sampled at 15 kHz during ten consecutive 20 second trials, in which a 1 second cis-3-hexanol or apple odor pulse was applied to the antenna. Single-unit measurements were made with devices inserted in the antennal lobe, which contains excitatory projection neurons that are known to respond to odor stimuli (Laurent and Davidowitz 1994). The probe was inserted at a maximum speed of ~10 μm/s, and lowered to a final depth of 250-300 μm with respect to the tip, corresponding to approximately the length of the antennal lobe and the full span of the electrode array. Signals were fed to two custom-built 16 channel

head stages, followed by main stage amplifiers and band pass filters, before being stored for offline analysis. Fig. 2 shows representative multisite recordings captured with one of our devices. The high recording site density of our array facilitates measurement of the same unit at many sites on the array (Figs 2A and 2B). Single-unit clusters were identified using a spike sorting algorithm (Perez-Orive *et al.* 2002; Mazor and Laurent 2005), which involved analyzing signals from four electrodes ("tetrodes," Gray *et al.* 1995). The putative units obtained from several tetrode sets were then combined, while taking care to avoid double-counting units observed on multiple tetrodes. Raster plots of two projection neurons measured in parallel are shown in Fig. 2C. As a further demonstration of the probe's recording functionality, local field potentials (LFPs) were measured in the mushroom body (Fig. 2D), displaying characteristic odor-evoked oscillations. The odor-evoked responses of single-units and LFP were found to agree with previous studies employing extracellular measurements in the locust (Perez-Orive *et al.* 2002).

RESULTS

Dual-side electrode array

Figs. 3A and 3B show the noise-averaged spike waveforms of two putative projection neurons that were measured in parallel on both sides of a dual-side array. The device was 25 μm thick. Signals from the first unit were strongest on the front, but some waveforms also display substantial amplitude on the back. In contrast, the second unit is measured almost exclusively with back-facing sites. Fig 3. leads to two salient observations: that extracellular fields decay on the scale of tens of microns beyond the presumed vicinity of the neuron (Henze *et al.* 2000); and that the device thickness may not be the only factor responsible for the amplitude asymmetry between the two sides. The addition of recording sites on the back may therefore increase the overall amount of measurable spike activity in a region of interest, thereby providing more useful information than single-side arrays without further disruption to tissue.

In order to gain further insight into the significance of signal amplitude asymmetries in dual-side arrays, we compared amplitude decay profiles that were measured from the same side, to those from opposite side of the array. Fig. 4A shows the normalized spike amplitude as a function of separation from

the site of maximum measured amplitude (V_0). The results display a high degree of variability, but suggest some important trends. In particular, signals from the V_0 side (blue points) decayed more slowly than those from the opposite side (red points). Moreover, the amplitude was found to drop by ~40 % at a distance of 25 μm on the V_0 side, whereas it was ~80 % attenuated at the same relative separation on the opposite side. This asymmetry is likely due to extracellular current shielding at the substrate-fluid interface (Perlin and Wise 2004; Moffitt and McIntyre 2005). A consequence of this effect is that dual-side arrays may routinely detect more units in the implanted region than their single-side counterparts.

Fig. 4A also suggests that on average, extracellular fields on the same side of the array decay in roughly inverse proportion to distance. We approximate the normalized peak-to-peak signal measured by an electrode as:

$$V_{pp} / V_0 = [1 + (x_r / \lambda)^n]^{-1} \quad (1)$$

where x_r is the radial distance from the electrode, λ is a characteristic decay length. The best fit of Eqn. 1 to the points in Fig. 4A gave values of λ = 33±2 μm and n = 1.4±0.2. Similar characteristic length scales have been reported elsewhere (Gray *et al.* 1995; Segev *et al.* 2004). Furthermore, the exponent closely matches the value that was obtained by Gold *et al.,* 2007.

Noise in extracellular measurements

Recording yield – the number of well-isolated single units – is affected by the presence of voltage noise in the measurement. Electric potential fluctuations primarily arise from three sources: (i) in the amplifier electronics and external electromagnetic interference, (ii) at the electrode-fluid interface, and (iii) in the brain in the form of unsorted background activity. The combination of these processes is manifested as the total measured noise, and is given by:

$$\delta V_{tot}^2 = \delta V_{amp}^2 + \delta V_{electrode}^2 + \delta V_{brain}^2 \quad (2)$$

For the measurements used to produce Fig. 4A, the total root mean square (RMS) noise was found to be 15±5 μV in the 300 to 5000 Hz band. By comparing values with the amplifier first shorted, and then

connected to electrodes immersed in locust saline, we determined that δV_{amp} = 4±1 μV, $\delta V_{electrode}$ = 5±1 μV, and by process of elimination, δV_{brain} = 14±6 μV. Next we assume a reliable detection event requires the peak-to-peak amplitude of a spike to exceed ~5δV_{tot}, which corresponds to ~75 μV_{pp} on at least one channel. This estimate is in close agreement to the actual lowest sortable spike amplitude (Fig. 4B) of 68 μV_{pp}. We found that only 16 out of a total of 73 single-units recorded with the dual-side array satisfied the above minimum amplitude criterion with channels on both sides of the array. Thus the likelihood of detecting the same spike simultaneously on both sides of the array is 22 %.

As noise in the system increases, the effective spike detection volume around an electrode is diminished. Using the best fit parameters to Eqn. 1, and $\langle V_0 \rangle$ = 204 μV, we estimate in Fig. 4C the average detection range per electrode, *r*, as a function of measurement noise. At the noise level of the antennal lobe, we estimate *r* to be ~40 μm. However, we note that differences in both δV_{brain} – which may reflect local inhomogeneities in firing activity – as well as extracellular fluid resistivity, could give rise to significant variations in detection range. Noise has been found to differ by about a factor of 4 throughout the cat cortex (Buchwald and Grover 1970).

The greatest barriers to extracellular current propagation between the front and back sides of dual-side arrays are likely to be the oxide and parylene insulation films; these highly resistive layers are necessary for ensuring proper channel isolation. It is therefore unclear whether further reduction in the shaft's cross section would ameliorate the suggested shielding effect. An alternative approach may be, where possible, to target regions that manifest less measurement noise. For example, in the absence of noise processes contributing to δV_{brain}, we estimate the upper bound for the detection radius to be ~140 μm. This upper bound is similar to an estimate obtained by a different method using multisite probe measurements in the rat hippocampus (Henze *et al.* 2000; Shoham *et al.* 2006). Moreover, under these highly optimal conditions the likelihood of simultaneously detecting a spike from both sides of our dual-side array would increase to about 58 %.

Double-layer electrode array

The 2 *x* 2 shaft microstructure, depicted in Fig. 1D, was designed to measure extracellular signals from the enclosed volume of tissue. This probe was tested successfully, as shown by the single-unit spike activity in Fig. 5A. The waveforms reveal an inhomogeneous spatial dependence of potential along the *x-y* and *x-z* sampling planes. A qualitative comparison of this observation with models of extracellular potential around a spiking neuron (Gold *et al.* 2006), suggests extensive branching of neuronal processes. This appears to be consistent with the radial secondary dendritic geometry of antennal lobe projection neurons (Laurent and Naraghi 1994).

The 3D geometry of the double-layer array raises the prospect for localizing the source of extracellular fields within the enclosed space. Fig. 5B displays the calculated center-of-field positions of two simultaneously recorded single-units. A more detailed description of the analysis method is provided in the Appendix. The majority of points in each cluster are concentrated in roughly spherical regions of diameter ~10 μm. This suggests that single-units can be localized with a spatial resolution comparable to the cell body size. Moreover, the usage of multilayer arrays in combination with more sophisticated analysis techniques could eventually enable tracking of signal propagation in the brain, and facilitate the study of neuronal interactions in cell assemblies (Barthó *et al* 2004; Blanche *et al* 2005).

DISCUSSION

Spatial resolution of 3D recordings

Our results, while acquired from relatively simple structures, establish the feasibility of achieving dense extracellular measurements with three geometric degrees of freedom, using dual-side and multilayer electrode arrays. A notable advantage of our dual-side array design is that the electrodes on each side are connected to separately accessible recording channels. A different design (Perlin and Wise 2005), can accommodate a single channel per unit area on the shaft, which can either be converted into a front, back, or double-sided electrode via the use of through-hole etch techniques. Double-sided electrodes that simultaneously sample both sides of the array average the signal between the front and

back facing sites; this makes signals susceptible to attenuation in the presence of asymmetric fields. On the other hand, while our approach requires twice as many channels per unit area, it is not susceptible to attenuation from averaging, and enables up to a twofold higher sampling density. The fine scale resolution provided by our dual-side arrays is viewed as an important feature for maximizing the recording yield from sparsely firing thin laminar structures in the brain. It is also intriguing to consider the possibility of using multilayer structures to perform dual stimulation and recording trials with a high degree of spatial precision. Such investigations may provide additional insight into single-cell level effects of electrical stimulation on brain function (McIntyre *et al.* 2004).

We envision merging the dual-side and multilayer device modalities and extending them toward more complex 3D microstructures aimed at large scale recording applications. However, the limited number of input channels on the electronics imposes a tradeoff between spatial sampling density and sampling volume, which can be tailored by adjusting the electrode and shaft spacing. The devices presented here were intended for fine scale spatial resolution and small volume measurements, which may be most useful for probing single or few cell phenomena in great detail. A slightly lower sampling density and larger volume may be ideal for exploring structure-function relationships in moderately sized structural units of neuronal ensembles, such as cortical columns (Mountcastle 1997). Such devices could also be used to map extracellular current source density in 3D in order to characterize information flow within and between multiple structures (Bragin *et al.* 1995). Finally, large, coarse scale studies may be the most practical method for functional mapping of mm^3 level volumes, and may present a complementary approach to functional magnetic resonance imaging, whose spatial resolution is limited to ~1 mm^3 and temporal resolution does not enable single-spike detection (Logothetis *et al.* 2001). They may also hold promise as an alternative method to voltage sensitive dye imaging (Mann *et al.* 2005), by enabling access to regions deep inside the brain without the need for using slices.

Fig. 6A represents a cross section of the basic structural component of a proposed large scale 3D microelectrode array. The device consists of 8 *x* 8 shafts and features both dual-side and multilayer modalities. The width and thickness of the shafts are assumed to be equal (*w*), and the nearest shaft

spacing (d) is the same along the vertical and horizontal axes. The detection volumes surrounding the electrodes are approximated as hemispheres, whose radius r is equivalent to the spike detection range estimated in Fig. 4C. Each shaft contains only one recording site on the front as well as the back side of each shaft, and is therefore best suited for moderate to coarse spatial scale measurement applications. In order to increase the depth of tissue probed by the 3D structure, the unit module (length $2r$) can be replicated along the longitudinal axis of the shafts. However, since all components are assumed to be identical, it is sufficient to consider a single module in the treatment that follows.

Ultimate limitations of 3D extracellular recordings

As the scale and complexity of the implanted structure increases, the risk of disrupting physiological brain activity is likely to rise. This suggests that two fundamental system design constraints are the amount of tissue damaged by the silicon microstructure, and the volume accessible for measurement. The former constraint requires small shafts and large shaft spacing, while the latter requires a large SNR and densely packed electrodes.

Using an intermediate value of 100 μm as the estimate for r, we predict in Fig. 6B the unique (i.e., non-overlapping) fractional volume in the entire array that should lie within range of detection. The fractional recording volume increases with smaller shaft separation until the condition $d \leq r$ is satisfied, at which point significant overlap occurs between adjacent patches. Fig. 6C shows the percentage of tissue displaced by the implant as a function of shaft spacing. The actual level of functional disruption may be considerably more complex than what is described by a simple volumetric estimate (Claverol-Tinture and Nádasdy 2004; Polikov *et al.* 2005); however, the fractional displacement volume provides a lower bound on the proportion of damaged cells expected to occur in the implanted region.

The above discussion on design limitations can help estimate the recording yield of the next generation of 3D microstructures. As an example, we consider an 8 x 8 shaft device in which the structural dimensions are reduced to w = 25 μm (Najafi *et al.* 1990) through the use of nanofabrication techniques. A shaft spacing of d = 200 μm would displace 2 % of the structure's volume, which is similar to the value

of some other implanted systems (Campbell *et al.* 1991; Bai *et al.* 2000). Assuming r = 100 μm, a 1 mm long device would use 5 modular sections (since each module is 200 μm long), bringing the total number of required data channels to 640. About 40 % of the 1.8 *x* 1.8 *x* 1 mm^3 enclosed volume would lie within the detection radius of an electrode. Based on previous investigations, one typically detects only 1 to 10 % of total available neurons in a selected region (Shoham *et al.* 2006). Hence given a neuronal density of 50,000 per mm^3 we would expect to measure between 650 and 6,500 units in 3.2 mm^3 of cortex. It thus appears that devices employing dual-side and multilayer arrays could enable an unprecedented scale of recordings in a spatially confined region. Future work needs to address the challenges of ensuring a minimally disruptive interface of 3D silicon microstructures with the brain.

APPENDIX

Electrical crosstalk and signal attenuation effects

Stray capacitive coupling is one of the factors that affect the performance of extracellular recordings. In order to characterize these effects on the fabricated microelectrode arrays, a model was developed using a general purpose analog electronic circuit simulator (SPICE). The equivalent circuit is depicted in Fig. A1. The model is qualitatively similar to that used by Najafi *et al.* (1990), but here we distinguish between two probe configurations: (i) crosstalk between adjacent traces on the same side of a shaft, and (ii) crosstalk between opposing traces on a dual-side or double-layer structure. It is assumed that the conductive Si device substrate is grounded when inserted in the extracellular milieu. In Fig. A1 we show the percentage of crosstalk ($V_{out,2}/V_{out,1}$) and signal transmission ($V_{out,1}/V_{in}$) as a function of equivalent electrode impedance. The results predict that with an electrode impedance of 0.25 MΩ, crosstalk should be $\leq$ 0.6 % in both configurations. Importantly, this value is insufficient to produce spurious spike detection events. Moreover, capacitive shunting of the signal transmission path to the extracellular fluid gives rise to an attenuation of ~3 %, the majority of which is due to the input capacitance at the headstage. Note that signal attenuation in configurations 1 and 2 is the same to within ~0.5 % for electrode impedance less than 1 MΩ, and we present only the worst case values, which correspond to configuration 2.

The relevant circuit parameters were defined as follows:

V_{in} is the simulated extracellular signal – a 1 kHz sine wave.

V_{out} is the simulated signal as measured after the preamplifier input.

R_s is the spreading resistance which is encountered by current spreading out into fluid in the electrode vicinity (Franks *et al.* 2005). R_s was calculated to be ~10 kΩ.

$R_{electrode}$ and $C_{electrode}$ are the equivalent resistive and capacitive components of the electrode impedance, respectively. These parameters were varied such that the net parallel electrode impedance ranged from 10 kΩ to 5 MΩ.

R_{ma} is the resistance of the metallic traces between the recording site and the input to the preamplifier. R_{ma} was measured to be ~500 Ω.

C_{sub} is the capacitive coupling to the extracellular fluid through the parylene C and thermal oxide layers. C_{sub} was estimated to be ≤ 2.7 pF.

$C_{cp,ij}$ is the coupling on the silicon *probe* between channels *i* and *j*. In the case of adjacent traces on the *same side* of a shaft (Configuration 1), $C_{cp,ij}$ = 0.1 pF. In the case of traces on either *opposite sides* of a dual-side shaft, or *opposite layers* of a double-layer shaft (Configuration 2), $C_{cp,ij} \leq 2.7$ pF.

$C_{cf,ij}$ is the coupling on the *flexible cable* between channels i and j. This was estimated to be ≤ 1 pF.

C_{amp} is the input capacitance at the headstage, and equals 12 pF.

3D spike source localization

In order to show spatial separation of spikes with the 3D probe, we first carried out tetrode-based spike sorting to identify the single-unit clusters. Treating each cluster separately, we then determined the center of field (COF) position for all spike events via the expression:

$$\vec{x}_j = \sum_i^n \vec{u}_i A_{ji} \Big/ \sum_i^n A_{ji} \tag{A1}$$

where $\vec{u}_i$ are the coordinates of the i^{th} electrode, and A_{ji} is the peak-to-peak amplitude observed for spike *j* at electrode *i* (Nádasdy *et al.* 1998).

ACKNOWLEDGEMENTS

JD and SCM thank Christof Koch for advice and support. We also thank Stijn Cassenaer, Zoltan Nadasdy, Ueli Rutishauser, Thanos Siapas, Mikko Vähäsöyrinki, and Hang Xu for discussions and technical assistance, and Michael Walsh and Timothy Heitzman for electronic hardware. Device fabrication was carried out at the Kavli Nanoscience Institute, Caltech, and the National Nanotechnology Infrastructure Network, University of California, Santa Barbara.

GRANTS

This work was funded by the Broad Fellows Program in Brain Circuitry (JD and SCM), the Della Martin Foundation and the Beckman Foundation (IHRK), and NIDCD (GL).

REFERENCES

Bai Q, Wise KD, Anderson DJ. A high-yield microassembly structure for three-dimensional microelectrode arrays. *IEEE Trans Biomed Eng* 47: 281-289, 2000.

Barthó P, Hirase H, Monconduit L, Zugaro, M, Harris KD, Buzsáki G. Characterization of neocortical principal cells and interneurons by network interactions and extracellular features. *J Neurophysiol* 92: 600-608, 2004.

Blanche TJ, Spacek MA, Hetke JF, Swindale NV. Polytrodes: high-density silicon electrode arrays for large-scale multiunit recording. *J Neurophysiol* 93: 2987-3000, 2005.

Bragin A, Jandó G, Nádasdy Z, Hetke J, Wise K, Buzsáki G. Gamma (40-100 Hz) oscillation in the hippocampus of the behaving rat. *J Neurosci* 15: 47-60, 1995.

Buchwald JS, Grover FS. Amplitudes of background fast activity characteristic of specific brain sites. *J Neurophysiol* 33: 148-159, 1970.

Buzsáki G. Large-scale recording of neuronal ensembles. *Nature Neurosci* 7: 446-451, 2004.

Campbell PK, Jones KE, Huber RJ, Horch KW, Normann RA. A silicon-based, three-dimensional neural interface: manufacturing processes for an intracortical electrode array. *IEEE Trans Biomed Eng* 38: 758-768, 1991.

Claverol-Tinture E, Nadasdy Z. Intersection of microwire electrodes with proximal CA1 stratum-pyramidale neurons at insertion for multiunit recordings predicted by a 3-D computer model. *IEEE Trans Biomed Eng* 51: 2211-2216, 2004.

Csicsvari J, Henze DA, Jamieson B, Harris KD, Sirota A, Barthó P, Wise KD, Buzsáki G. Massively parallel recording of unit and local field potentials with silicon-based electrodes. *J Neurophysiol* 90: 1314-1323, 2003.

Franks W, Schenker I, Schmutz P, Hierlemann A. Impedance characterization and modeling of electrodes for biomedical applications. *IEEE Trans Biomed Eng* 52: 1295-1302, 2005.

Gray CM, Maldonado PE, Wilson M, McNaughton B. Tetrodes markedly improve the reliability and yield of multiple single-unit isolation from multi-unit recordings in cat striate cortex. *J Neurosci Methods* 63: 43-54, 1995.

Gold C, Henze DA, Koch C, Buzsáki G. On the origin of the extracellular action potential waveform: a modeling study. *J Neurophysiol* 95: 3113-3128, 2006.

Gold C, Henze DA, Koch C. Using extracellular action potential recordings to constrain compartmental models. *J Comput Neurosci* 23: 39-58, 2007.

Henze DA, Borhegyi Z, Csicsvari J, Mamiya A, Harris KD, Buzsáki G. Intracellular features predicted by extracellular recordings in the hippocampus in vivo. *J Neurophysiol* 84: 390-400, 2000.

Hoogerwerf AC, Wise KD. A three-dimensional microelectrode array for chronic neural recording. *IEEE Trans Biomed Eng* 41: 1136-1146, 1994.

Laurent G, Davidowitz H. Encoding of olfactory information with oscillating neural assemblies. *Science* 265: 1872-1875, 1994.

Laurent G, Naraghi M. Odorant-induced oscillations in the mushroom bodies of the locust. *J Neurosci* 14: 2993-3004, 1994.

Logothetis NK, Pauls J, Augath M, Trinath T, Oeltermann A. Neurophysiological investigation of the basis of the fMRI signal. *Nature* 412: 150-157, 2001.

Mann EO, Suckling JM, Hajos N, Greenfield SA, Paulsen O. Perisomatic feedback inhibition underlies cholinergically induced fast oscillations in the rat hippocampus in vitro. *Neuron* 45: 105-117, 2005.

Mazor O, Laurent G. Transient dynamics versus fixed points in odor representations by locust antennal lobe projection neurons. *Neuron* 48: 661-673, 2005.

McIntyre CC, Grill WM, Sherman DL, Thakor NV. Cellular effects of deep brain stimulation: model-based analysis of activation and inhibition. *J Neurophysiol* 91: 1457-1469, 2004.

Moffitt MA, McIntyre CC. Model-based analysis of cortical recording with silicon microelectrodes. *Clin Neurophysiol* 116: 2240-2250, 2005)

Mountcastle VB. The columnar organization of the neocortex. *Brain* 120: 701-722, 1997.

Nádasdy Z, Csicsvari J, Penttonen M, Hetke J, Wise K, Buzsáki G. Extracellular recording and analysis of neuronal activity: from single cells to ensembles. In: *Neuronal ensembles: strategies for recording and decoding.* EichenbaumH, Davis JL (eds), New York: Wiley, 1998, p. 17-55.

Najafi K, Wise KD, Mochizuki T. A high-yield IC-compatible multichannel recording array. *IEEE Trans Electron Devices* 32: 1206-1211, 1985.

Najafi K, Ji J, Wise KD. Scaling limitations of silicon multichannel recording probes. *IEEE Trans Biomed Eng* 37: 1-11, 1990.

Nicolelis MAL, Ghazanfar AA, Faggin BM, Votaw S, Oliveira LMO. Reconstructing the Engram: simultaneous, multisite, many single neuron recordings. *Neuron* 18: 529-537, 1997.

Neves HP, Orban GA, Koudelka-Hep M, Stieglitz T, Ruther P. Development of modular multifunctional probe arrays for cerebral applications. *Proc 3rd Intl IEEE EMBS Conference Neural Eng* 104-109, 2007.

Olsson RH, Buhl DL, Sirota AM, Buzsáki G, Wise KD. Band-tunable and multiplexed integrated circuits for simultaneous recording and stimulation with microelectrode arrays. *IEEE Trans Biomed Eng* 52: 1303-1311, 2005.

Pang C, Cham JG, Nenadic Z, Mussallam S, Tai YC, Burdick JW, Andersen RA. A new multi-site probe array with monolithically integrated parylene flexible cable for neural prostheses. *27th Intl Conf IEEE Eng in Med and Biol Soc (EMBS)*, 2005.

Perez-Orive J, Mazor O, Turner GC, Cassenaer S, Wilson RI, Laurent G. Oscillations and sparsening of odor representations in the mushroom body. *Science* 297: 359-365, 2002.

Perlin GE, Wise KD. The effect of the substrate on the extracellular neural activity recorded with micromachined silicon microprobes. *Proc 26th Intl Conf IEEE-EMBS* 2002-2005, 2004.

Polikov VS, Tresco PA, Reichert WM. Response of brain tissue to chronically implanted neural electrodes. *J Neurosci Methods* 148: 1-18, 2005.

Segev R, Goodhouse J, Puchalla J, Berry MJ. Recording spikes from a large fraction of the ganglion cells in a retinal patch. *Nature Neurosci* 7: 1155-1162, 2004.

Shoham S, O'Connor DH, Segev R. How silent is the brain: is there a "dark matter" problem in neuroscience? *J Comp Physiol A* 192: 777-784, 2006.

Wise KD, Sodagar AM, Yao Y, Ning Gulari M, Perlin GE, Najafi K. Implantable neural microsystems. *Proc IEEE* 96: 1184-1202, 2008.

Yao Y, Ning Gulari M, Wiler JA, Wise KD. A microassembled low-profile three-dimensional microelectrode array for neural prosthesis applications. *J MEMS* 16: 977-988, 2007.

FIGURE LEGENDS

FIG. 1. Dual-side and double-layer microelectrode arrays were built on thin silicon shafts. (A) Front view of the device. The shaft dimensions are 4 mm x 70 μm x 50 μm (*l* x *w* x *t*). Sealing epoxy is visible at the base of the structure. (B) Expanded view of the front and back side (left and right images, respectively) of the dual-side array. The recording sites have a geometric area of 100 μm^2. (C) Layers involved in connecting dual-side arrays to flexible printed circuit boards (green); one board for each side. Electrical connections were made via low profile flip-chip bonds. (D) View of the tip of a 2 x 2 shaft, double-layer array. (E) A modular assembly scheme was employed to make the multilayer structure. Note that the PCB contained conducting leads on both sides, and thus the same board connected to the upper recording sites on the bottom layer and the lower sites on the top layer. With this approach the enclosed volume was sampled with two opposing sets of recording arrays.

FIG. 2. The dual-side microelectrode array enabled multisite recordings of spike activity in the locust antennal lobe. (A) Segments from 4 simultaneously recorded channels located on the same array. Signals were sampled at 15 kHz, and filtered from 300 to 5000 Hz. Channels 1-4 are located on the back side. (B) Superimposed spike waveforms from a putative projection neuron. The data segments were triggered on spike times from Ch. 4. The solid black lines represent the averaged waveform. (C) Raster plot of three putative projection neurons that were recorded in parallel. Ten consecutive trials are shown for each cell. The gray bar indicates a 1 second cis-3-hexanol odor presentation to the antenna. (D) A recording site on the dual-side array faithfully measures local field potentials (LFP) in the mushroom body. The site is located at the tip of the back side. The gray bar denotes a one second cis-3-hexanol odor presentation. Data represent three consecutive single-channel trials, filtered from 5 to 300 Hz.

FIG. 3. Spike activity was measured in parallel on both sides of a 25 μm thick dual-side microelectrode array. Mean spike-triggered waveforms from two putative single-units are displayed beside an edited representation of their corresponding electrodes on the front (A) and back (B) side of the array. For clarity, traces for units 1 and 2 were offset along the vertical axis. Vertical gray lines denote the same point in time for each unit.

FIG. 4. Extracellular action potential fields appear strongly attenuated by probe shielding effects. (A) Normalized spatial decay profiles of 73 single-unit that were recorded with a 25 μm thick dual-side array. Blue dots represent signals from the side displaying the highest average amplitude for a selected unit. The dashed blue curve is a fit to these points using Eqn. 1, which gives a characteristic decay length of λ = 33±2 μm (R^2 = 0.72). Red dots represent measurements from the opposite, weaker signal side of the array, and the dashed red line, which is intended as a rough visual guide, is a straight-line fit to those points. (B) Histogram of the maximum measured spike amplitude, V_0, of each single-unit recorded with dual-side arrays. The mean value is 204±125 μV_{pp}. (C) Estimate of spike detection range as a function of total noise in the measurement. The assumptions used to model the effective range were that λ = 33 μm, the average maximum spike amplitude V_0 is 204 μV_{pp}, and that $V_{pp} \geq 5\delta V_{tot}$ is required to detect a spike.

FIG. 5. The double-layer array device measured the extracellular potential of a projection neuron in 3D. (A) A graphical representation of the device was used showing 16 functional electrodes. Shafts were 50 μm thick. The mean spike-triggered waveforms from a single-unit ("Unit 1"), were placed next to their corresponding color-matched recording sites. Dashed vertical gray lines denote the same point in time. An additional 8 electrodes (gray rectangles) were not used in the measurements, and for clarity the top left shaft was omitted from the diagram. Note that all sites faced inward and therefore sampled the same volume. The shaded sphere represents the approximate center of field (COF) position of the field source. (B) 3D spike source localization of two simultaneously measured single-units. Spike events belonging to Cluster 1 were used to produce the averaged waveforms of Unit 1 in (A), while the waveforms of Cluster

2 were not depicted. Gray lines converge at the COF positions. Note that coordinates represent relative positions. Points in each 3D cluster are distributed ~5 μm from their respective average position, and centers are separated by 17 μm.

FIG. 6. Ultimate limitations of 3D extracellular recordings. (A) Graphical representation of the top (i) and 3D (ii) cross sectional views of the basic structural component of an 8 *x* 8 shaft array. Shafts (blue) have width and thickness *w*, and nearest neighbor spacing *d*. The violet shaded hemispheres, radius *r*, represent the approximate detection volume surrounding each electrode. Arrays containing multiple modular components would have vertical electrode spacing of 2*r*. (B) and (C) represent the fractional detection volume and fractional displacement volume as a function of shaft spacing *d*. An assumption used in (B) is that $w = 25$ μm. The total volume is indicated by the dashed lines surrounding the module in (A).

FIG. A1. Analysis of electrical crosstalk and signal attenuation effects. (A) Equivalent device circuit model of adjacent recording channels. Configuration 1 (the full depicted circuit) corresponds to adjacent traces on the same side of a shaft. The dashed box denotes Configuration 2, which corresponds to opposing traces on a dual-side or double-layer array. (B) SPICE simulation results of crosstalk and signal transmission for the two configurations.

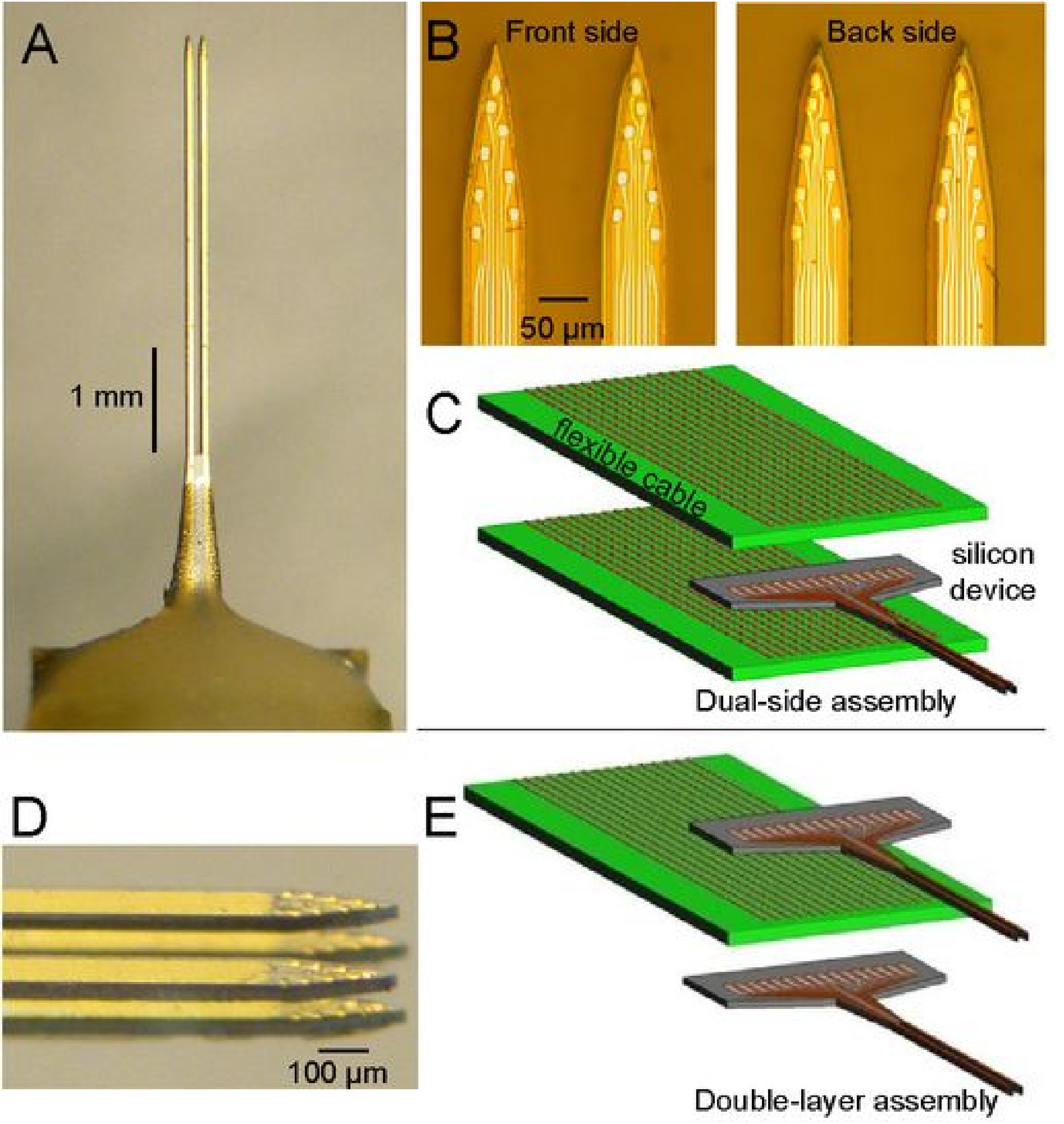
A
1 mm
B
Front side
50 µm
Back side
C
flexible cable
silicon
device
Dual-side assembly
D
100 µm
E
Double-layer assembly

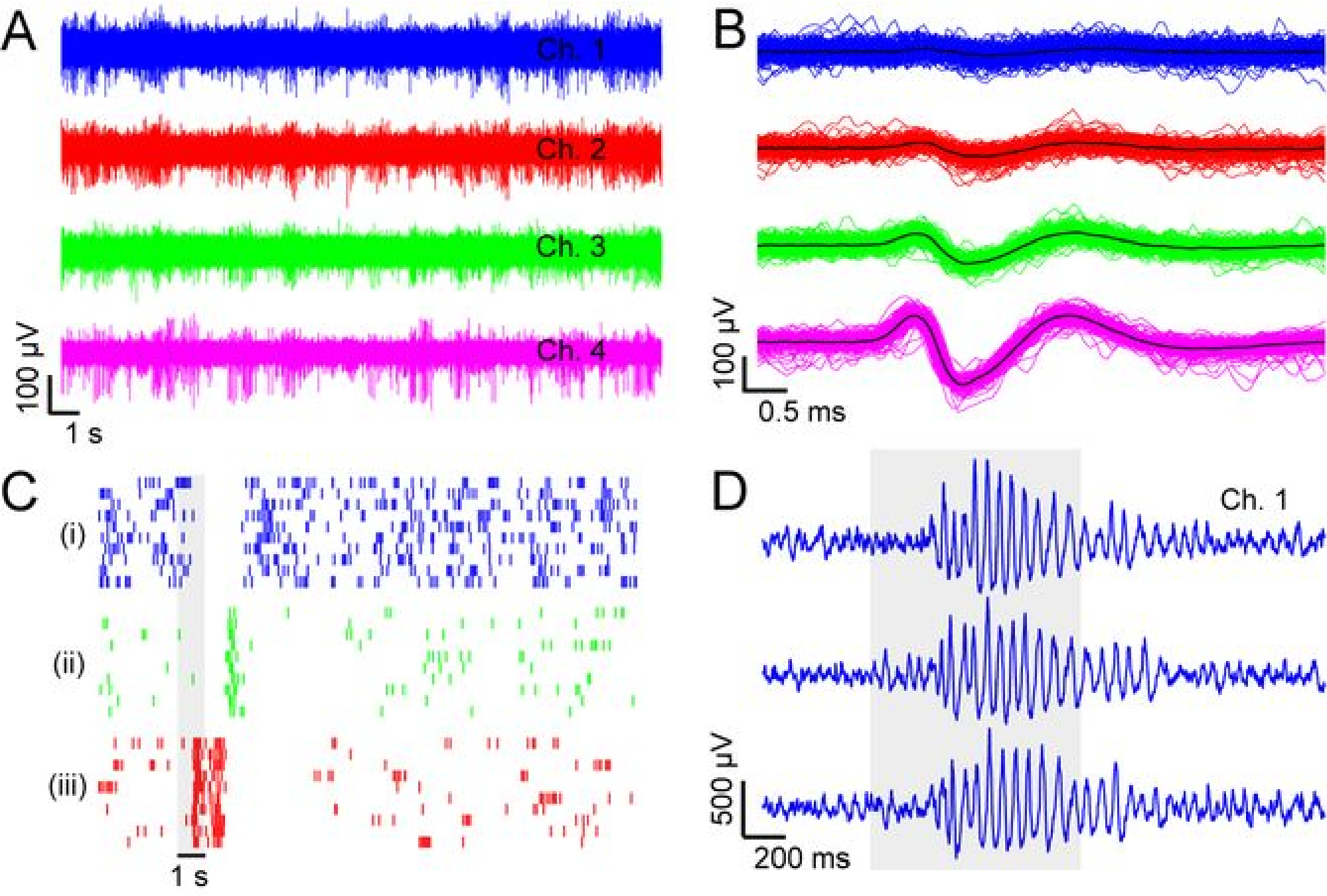
A
Ch. 1
Ch. 2
Ch. 3
Ch. 4
100 µV
1 s
B
100 µV
0.5 ms
C
(i)
(ii)
(iii)
1 s
D
Ch. 1
500 µV
200 ms

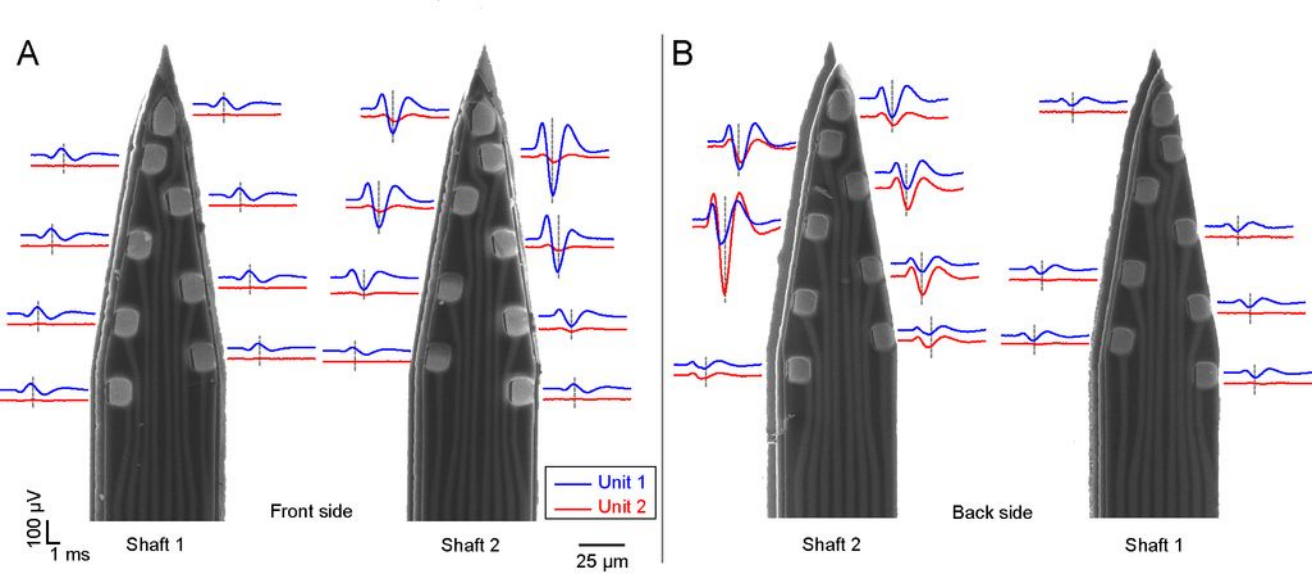
A
B
Unit 1
Unit 2
Front side
Back side
Shaft 1
Shaft 2
Shaft 2
Shaft 1
100 µV
1 ms
25 µm

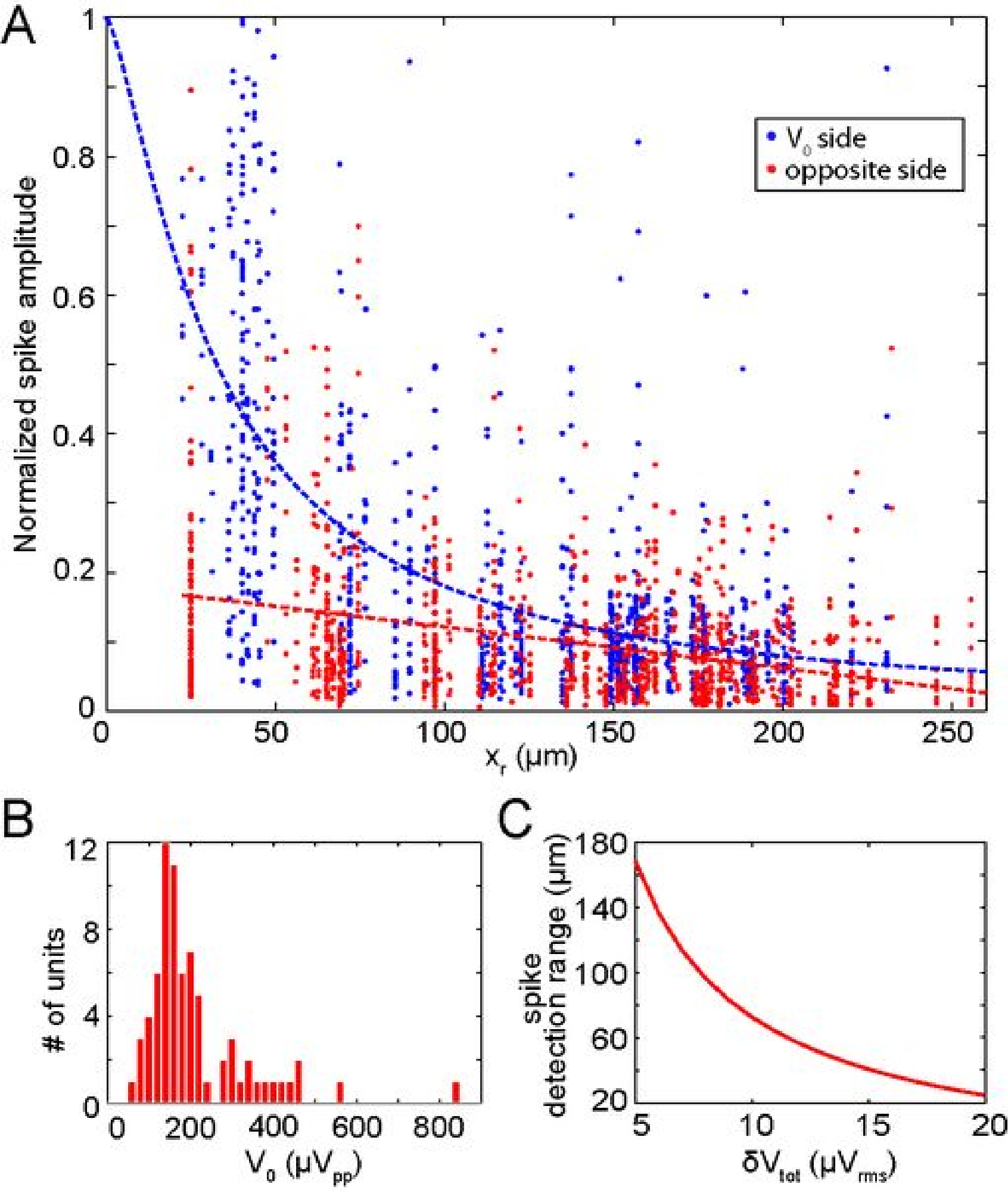
A
Normalized spike amplitude
1
0.8
0.6
0.4
0.2
0
0
50
100
150
200
250
x_r (μm)
V_0 side
opposite side
B
# of units
12
8
4
0
0
200
400
600
800
V_0 (μV_pp)
C
spike detection range (μm)
180
140
100
60
20
5
10
15
20
δV_tot (μV_rms)

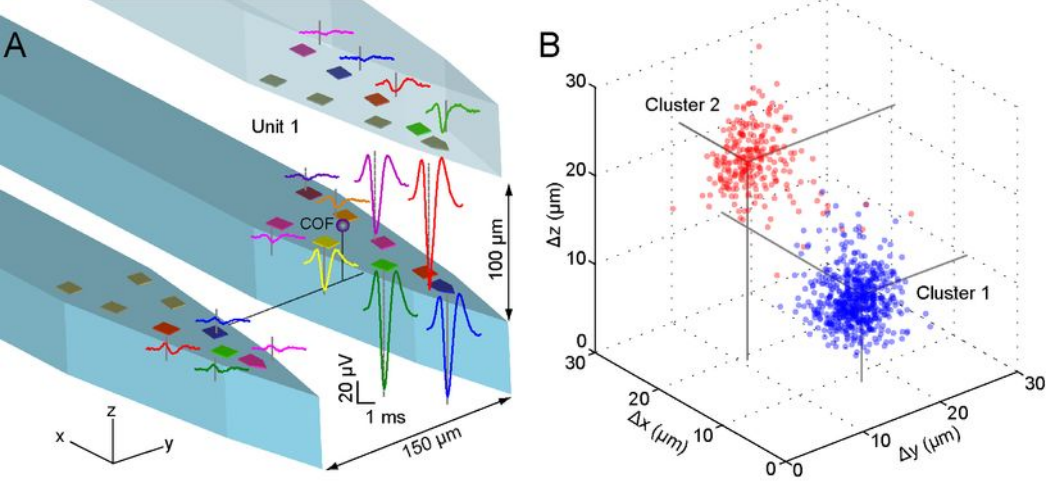
A
Unit 1
COF
100 µm
20 µV
1 ms
150 µm
z
x
y
B
Cluster 2
Cluster 1
Δz (µm)
Δx (µm)
Δy (µm)
30
20
10
0

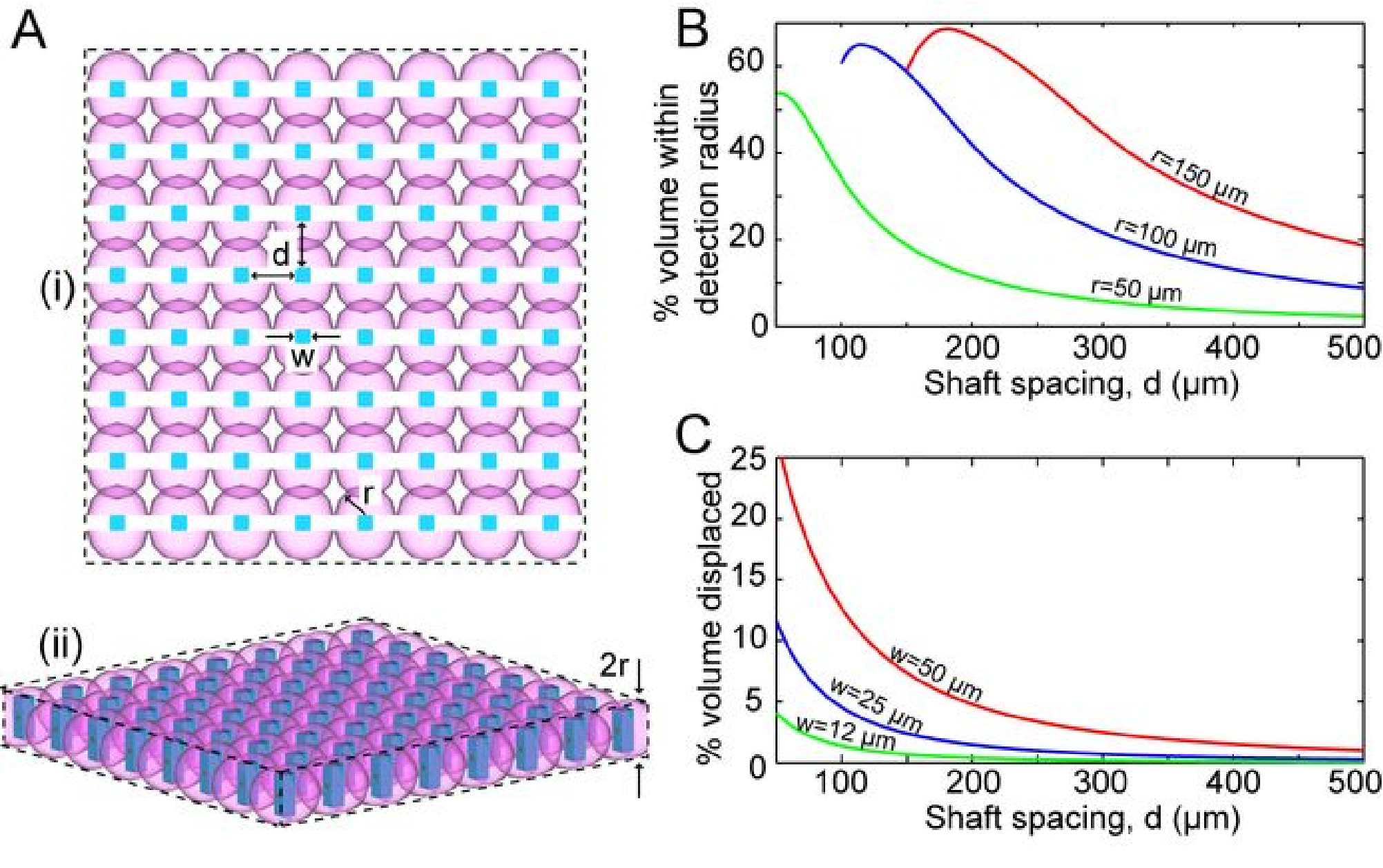
A
(i)
d
w
r
(ii)
2r
B
% volume within detection radius
60
40
20
0
100
200
300
400
500
Shaft spacing, d (μm)
r=150 μm
r=100 μm
r=50 μm
C
% volume displaced
25
20
15
10
5
0
100
200
300
400
500
Shaft spacing, d (μm)
w=50 μm
w=25 μm
w=12 μm

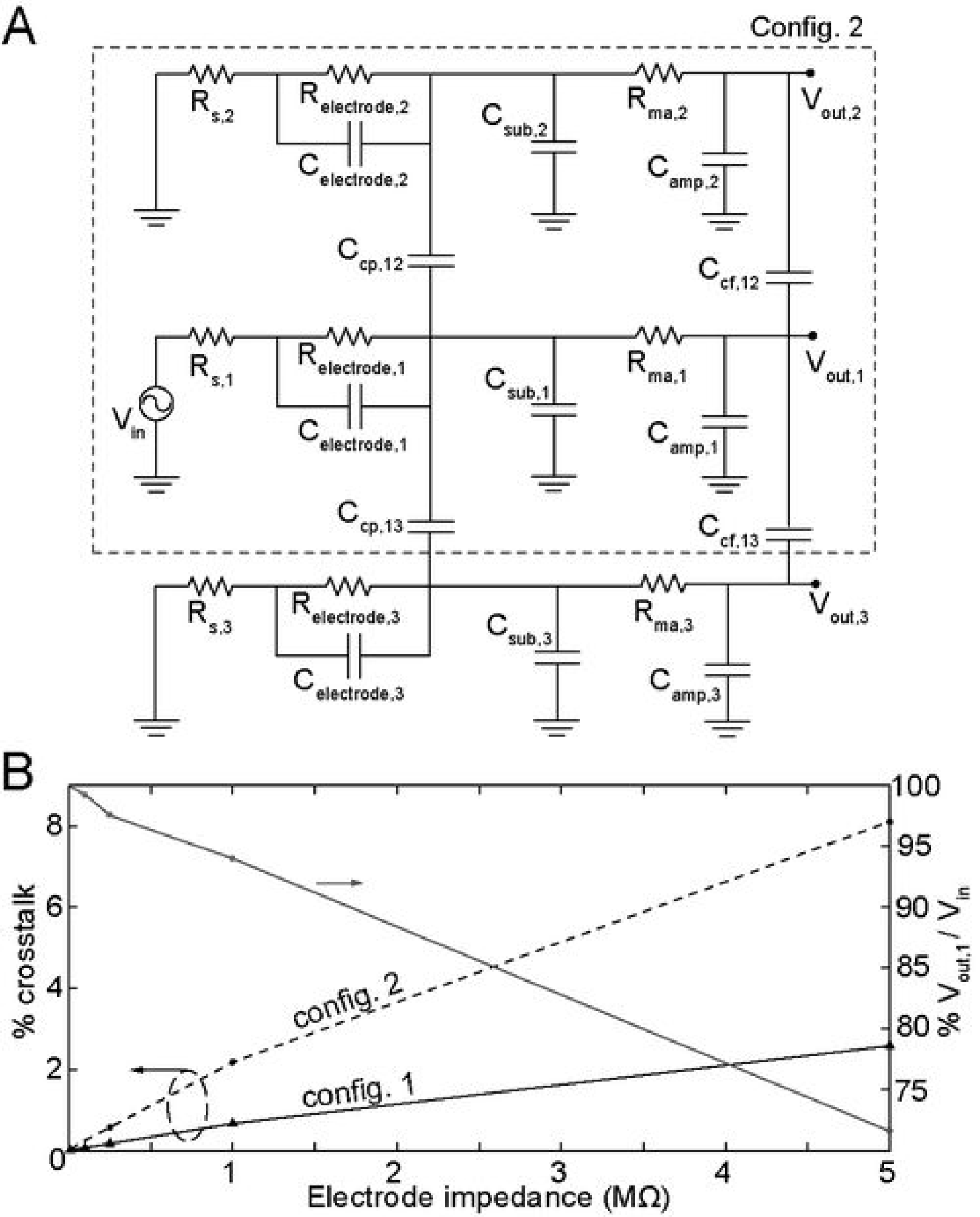
A
Config. 2
R s,2
R electrode,2
C electrode,2
C sub,2
R ma,2
V out,2
C amp,2
C cp,12
C cf,12
R s,1
R electrode,1
C electrode,1
V in
C sub,1
R ma,1
V out,1
C amp,1
C cp,13
C cf,13
R s,3
R electrode,3
C electrode,3
C sub,3
R ma,3
V out,3
C amp,3
B
% crosstalk
% V out,1 / V in
config. 2
config. 1
Electrode impedance (MΩ)
0
2
4
6
8
75
80
85
90
95
100
1
2
3
4
5